RESEARCH ARTICLES

STRUCTURAL BIOLOGY

A three-dimensional movie of structural changes in bacteriorhodopsin

Eriko Nango,[1,2] Antoine Royant,[3,4]* Minoru Kubo,[1,5]* Takanori Nakane,[6] Cecilia Wickstrand,[7] Tetsunari Kimura,[1,8] Tomoyuki Tanaka,[1] Kensuke Tono,[9] Changyong Song,[1,10] Rie Tanaka,[1] Toshi Arima,[1] Ayumi Yamashita,[1] Jun Kobayashi,[1] Toshiaki Hosaka,[11] Eiichi Mizohata,[12] Przemyslaw Nogly,[13] Michihiro Sugahara,[1] Daewoong Nam,[10] Takashi Nomura,[1] Tatsuro Shimamura,[2] Dohyun Im,[2] Takaaki Fujiwara,[2] Yasuaki Yamanaka,[2] Byeonghyun Jeon,[10] Tomohiro Nishizawa,[5,6] Kazumasa Oda,[6] Masahiro Fukuda,[6] Rebecka Andersson,[7] Petra Båth,[7] Robert Dods,[7] Jan Davidsson,[14] Shigeru Matsuoka,[15] Satoshi Kawatake,[15] Michio Murata,[15] Osamu Nureki,[6] Shigeki Owada,[1] Takashi Kameshima,[9] Takaki Hatsui,[1] Yasumasa Joti,[9] Gebhard Schertler,[13,16] Makina Yabashi,[1] Ana-Nicoleta Bondar,[17] Jörg Standfuss,[13] Richard Neutze,[7]† So Iwata[1,2]†

Bacteriorhodopsin (bR) is a light-driven proton pump and a model membrane transport protein. We used time-resolved serial femtosecond crystallography at an x-ray free electron laser to visualize conformational changes in bR from nanoseconds to milliseconds following photoactivation. An initially twisted retinal chromophore displaces a conserved tryptophan residue of transmembrane helix F on the cytoplasmic side of the protein while dislodging a key water molecule on the extracellular side. The resulting cascade of structural changes throughout the protein shows how motions are choreographed as bR transports protons uphill against a transmembrane concentration gradient.

Energy-coupled membrane transport proteins are ubiquitous in biology. The basic framework underpinning unidirectional membrane transport is called the alternating access model and was proposed by Jardetzky half a century ago (*1*). This theory postulates that a high-affinity binding site, which is initially accessible to one side of the membrane, is converted through structural changes into a low-affinity binding site that is accessible to the other side of the membrane (fig. S1). The recent advent of time-resolved serial femtosecond crystallography (TR-SFX) at an x-ray free electron laser (XFEL) (*2*–*4*) provides an opportunity to examine this framework.

Bacteriorhodopsin (bR) harvests the energy content of light to drive conformational changes leading to unidirectional proton transport. Energy stored within a transmembrane proton concentration gradient is converted by adenosine triphosphate (ATP) synthase into ATP or is coupled to other transport processes. Considerable effort has been made to understand how structural changes in bR transport a proton uphill against a transmembrane potential (*5*–*7*). Crystallographic structures derived from data recorded at cryogenic temperature reveal both light- and mutation-induced structural changes in bR (*6*, *7*), but this work is controversial for several reasons: (i) The reported structures show considerable variation (*7*), (ii) structures trapped at cryogenic temperature or by mutation do not correlate directly with time-dependent structural changes in wild-type bR, and (iii) x-ray induced radiation damage may mislead the interpretation of trapped intermediate structures (*8*–*10*). We circumvented these concerns by using TR-SFX to record a three-dimensional (3D) movie of structural changes in bR at room temperature at 2.1-Å resolution (*2*–*4*). We collected our data by using 10-fs-long XFEL pulses at the SPring-8 Angstrom Compact Free Electron Laser (SACLA). The principle of "diffraction before destruction" (*11*) ensures that these crystallographic structures are effectively free from the influence of x-ray–induced radiation damage (*12*).

Structure of the bR resting conformation

Bacteriorhodopsin is a seven-transmembrane α-helix protein containing a buried all-trans retinal chromophore that is covalently attached, through a protonated Schiff base (SB), to Lys^{216} of helix G. Light photoexcites the chromophore, which isomerizes with high quantum yield to a 13-cis configuration (Fig. 1A) and thereby initiates a sequence of spectral (fig. S2) and structural changes that facilitate spontaneous proton exchange between acidic and basic amino acid residues (Fig. 1B). Electron density for the resting-state bR structure (Fig. 1C; see also table S1 for crystallographic data) shows how the protonated SB forms a hydrogen-bond (H-bond) interaction with a water molecule, labeled Wat402 (*13*). This interaction is critical for attaining the high SB proton affinity with a pK_a of 13.3 (where K_a is the acid dissociation constant) (*14*). Asp^{85}, the primary proton acceptor, also forms an H-bond interaction with Wat402, and additional H-bond interactions with Thr^{89} and Wat401 ensure its low resting-state pK_a of 2.2 (*15*). A difference of 11 orders of magnitude between the proton affinities of the primary donor and acceptor prevents the leakage of protons from the extracellular (EC) medium to the cytoplasm (CP) but raises the question of what brings these proton affinities close together to facilitate spontaneous proton exchange? It is also puzzling why it takes microseconds for the primary proton transfer to occur when the SB and Asp^{85} are initially separated by only 4 Å and a water-mediated proton exchange pathway between these two groups is seen in the resting state (*13*). Moreover, protons are pumped from the CP to the EC, yet retinal isomerization redirects the SB proton away from the EC and toward the CP (Fig. 1A), which appears to contradict Jardetzky's framework.

Time-resolved spectroscopy studies of bR microcrystals

Before returning to the bR resting state, photoactivated bR progresses through a sequence of spectral intermediates labeled K, L, M_1 (early M), M_2 (late M), N, and O (fig. S2). A proton is transferred from the SB to Asp^{85} in the L-to-M transition and from Asp^{96} to the SB from the M-to-N transition. Time-resolved difference absorption spectra from bR microcrystals suspended in a lipidic cubic phase matrix (fig. S3A) show a photocycle turnover similar to that of

[1]RIKEN SPring-8 Center, 1-1-1 Kouto, Sayo-cho, Sayo-gun, Hyogo 679-5148, Japan. [2]Department of Cell Biology, Graduate School of Medicine, Kyoto University, Yoshidakonoe-cho, Sakyo-ku, Kyoto 606-8501, Japan. [3]Université Grenoble Alpes, CNRS, Commissariat à l'Energie Atomique et aux Energies Alternatives, Institut de Biologie Structurale, F-38044 Grenoble, France. [4]European Synchrotron Radiation Facility, F-38043 Grenoble, France. [5]Japan Science and Technology Agency (JST)–Precursory Research for Embryonic Science and Technology (PRESTO), 4-1-8 Honcho, Kawaguchi, Saitama 332-0012, Japan. [6]Department of Biological Sciences, Graduate School of Science, University of Tokyo, 2-11-16 Yayoi, Bunkyo-ku, Tokyo 113-0032, Japan. [7]Department of Chemistry and Molecular Biology, University of Gothenburg, Box 462, SE-40530 Gothenburg, Sweden. [8]Department of Chemistry, Graduate School of Science, Kobe University, 1-1 Rokkodai, Nada-ku, Kobe 657-8501, Japan. [9]Japan Synchrotron Radiation Research Institute, 1-1-1 Kouto, Sayo-cho, Sayo-gun, Hyogo 679-5198, Japan. [10]Department of Physics, Pohang University of Science and Technology, Pohang 790-784, Korea. [11]Division of Structural and Synthetic Biology, RIKEN Center for Life Science Technologies, 1-7-22 Suehiro-cho, Tsurumi-ku, Yokohama 230-0045, Japan. [12]Department of Applied Chemistry, Graduate School of Engineering, Osaka University, 2-1 Yamadaoka, Suita, Osaka 565-0871, Japan. [13]Division of Biology and Chemistry, Laboratory for Biomolecular Research, Paul Scherrer Institute, 5232 Villigen, Switzerland. [14]Department of Chemistry - Ångström Laboratory, Uppsala University, Uppsala, Sweden. [15]JST–Exploratory Research for Advanced Technology (ERATO), Lipid Active Structure Project, Osaka University, 1-1 Machikaneyama, Toyonaka, Osaka 560-0043, Japan. [16]Department of Biology, ETH Zurich, 8093 Zürich, Switzerland. [17]Theoretical Molecular Biophysics, Department of Physics, Freie Universität Berlin, Arnimallee 14, D-14195 Berlin, Germany.
*These authors contributed equally to this work. †Corresponding author. Email: richard.neutze@gu.se (R.N.); s.iwata@spring8.or.jp (S.I.)

wild-type bR in the purple membrane. Spectral decomposition reveals that for a time delay $\Delta t \leq 10$ μs, the photoactivated population in microcrystals is dominated by the L intermediate but with traces of K, whereas the M-intermediate population increases to 50% at $\Delta t = 19$ μs and falls to 50% at $\Delta t = 10$ ms (fig. S3, B and C). Measurements from four independent crystal batches yield the half-rise for the M-state as 15 ± 7 μs and the half-decay as 8 ± 3 ms.

Overview of structural rearrangements within the bR photocycle

In TR-SFX, a continuous stream of microcrystals is injected across a focused XFEL beam, and the delay between sample photoactivation and the arrival of an XFEL pulse is controlled electronically (*2*–*4*) (fig. S4). TR-SFX data were recorded to 2.1-Å resolution from light-adapted bR microcrystals after photoactivation by a nanosecond laser pulse for $\Delta t = 16$ ns, 40 ns, 110 ns, 290 ns, 760 ns, 2 μs, 5.25 μs, 13.8 μs, 36.2 μs, 95.2 μs, 250 μs, 657 μs, and 1.725 ms (table S1), which are evenly spaced on a logarithmic scale. A global overview of the evolution of difference electron density reveals how structural changes first emerge near the active site of the protein and become stronger around Lys^{216} of helix G and Trp^{182} of helix F before cascading toward the EC side of the protein along helix C (fig. S5 and movie S1).

Early structural changes in the bR photocycle

For $\Delta t = 16$ ns, which corresponds to essentially pure K intermediate, paired negative and positive difference electron density features adjacent to the C20 methyl group reveal that the retinal is initially tilted toward helix G in response to photoisomerization (Fig. 2A). Combined quantum mechanics and molecular mechanics computations also favor a twisted retinal geometry (fig. S6) and indicate that ~17 kcal/mol of energy is initially stored within this distorted active site configuration, which equates to 32% of the absorbed photon's energy and is compatible with earlier estimates (*16*, *17*). By $\Delta t = 290$ ns, the positive difference density feature associated with the C20 methyl is much weaker and moves into the plane of the retinal, whereas paired negative and positive difference electron density features associated with Trp^{182} grow stronger (Fig. 2B), showing how Trp^{182} is displaced toward the CP as the retinal straightens (Fig. 2C). Negative and positive difference electron density features also indicate that a movement of the side chain and backbone of Lys^{216} has begun at $\Delta t = 16$ ns (movies S2 and S3).

A strong negative difference electron density peak visible at $\Delta t = 16$ ns on Wat402 (Fig. 2A) shows that this water molecule is rapidly disordered by retinal isomerization. This feature doubles in strength as the photocycle evolves (Fig. 3A, movies S2 and S3, and table S2), indicating that the freedom of Wat402 to move is initially constrained by the limited size of the cavity in which it is buried. However, this water becomes increasingly mobile as the retinal is displaced toward the CP. Low-temperature trapping studies have suggested that Wat402 disorders upon retinal photoisomerization (*18*), but this conclusion was challenged in light of similar observations due to x-ray induced radiation damage (*8*–*10*). Because no effects of radiation damage are visible when using ≤10-fs XFEL pulses at an x-ray dose of 12 MGy (*12*, *19*), these TR-SFX data bring closure to this debate. It is noteworthy that one trapped K-intermediate showed Wat402 disordering (*18*) but did not visualize a twist of the retinal C20 methyl toward helix G (Fig. 2, A and C), whereas another captured this twist but kept Wat402 in the K-state model (*8*), and a third K-state structure showed neither change (*20*).

Conformational changes associated with proton transfer

The key step in achieving unidirectional proton transport by bR is the primary transfer event from the SB to Asp^{85} (the L-to-M transition) because only the mutation of Asp^{85} (*21*) or the removal of retinal completely stops proton pumping. Our data reveal a smooth evolution of electron density changes on the CP side of helices F and G before proton transfer (Fig. 3B and movies S1 and S3). Paired positive and negative density features also show that the side chain of Leu^{93} is displaced toward the CP and a weaker positive difference electron density peak arises between the retinal, Leu^{93}, and Thr^{89} from $\Delta t = 40$ ns until 13.8 μs (Fig. 4A) and is strongest at $\Delta t = 760$ ns (Fig. 3C and table S2). We modeled this feature as a transient water molecule [Wat452 (W452) in Fig. 4B] that shows weak H-bond interactions with the SB (3.35 Å) and the backbone carbonyl oxygen of Thr^{89} (3.35 Å). Its crystallographic distance to Oγ of Thr^{89} of 3.95 Å may also be classified as a weak H-bond interaction (*22*). Structural refinement shows that for $\Delta t = 16$ ns, Oγ of Thr^{89} is separated from the SB by 3.97 Å and the SB nitrogen is pointing toward helix G, whereas for $\Delta t = 760$ ns the SB nitrogen rotates almost 180° toward helix C and reduces the SB-Oγ separation to 3.30 Å. Fluctuations about these crystallographic positions could therefore create a transient proton-transport pathway linking the SB to Asp^{85} through Wat452 and Thr^{89} (Fig. 4B).

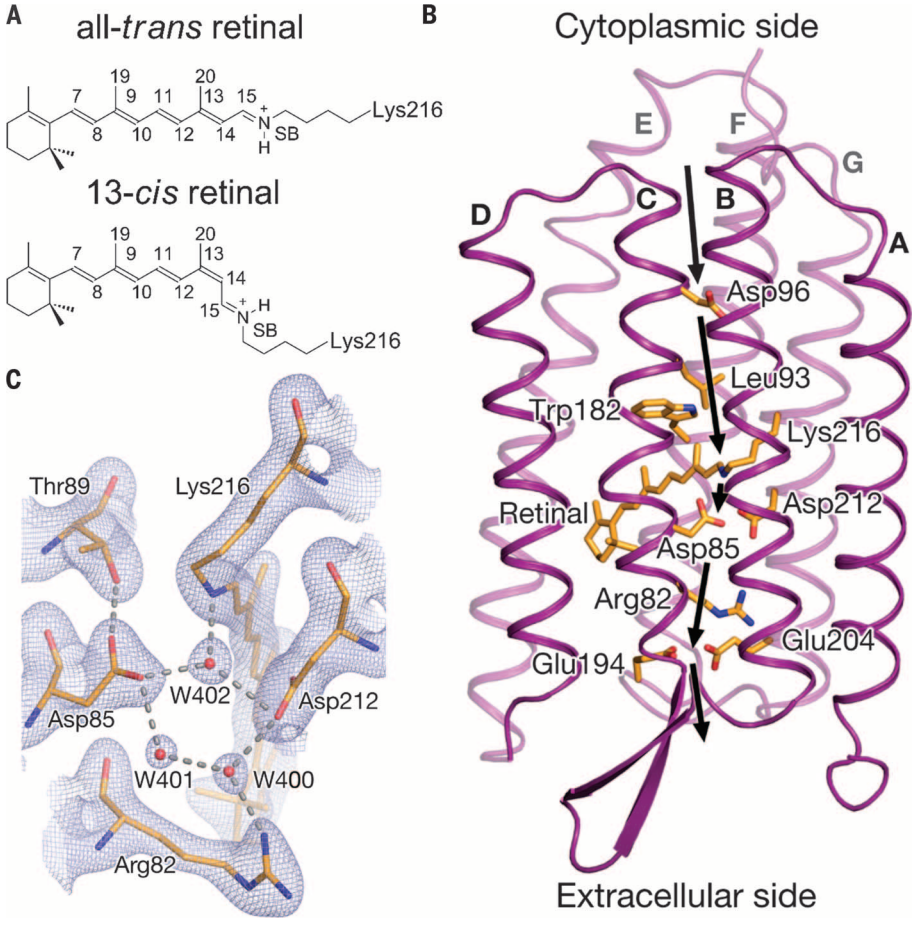

Fig. 1. Structure and function of bacteriorhodopsin (bR). (**A**) Schematic illustrating retinal covalently bound to Lys^{216} through a protonated Schiff base (SB) in an all-trans and a 13-cis configuration. (**B**) Proton-exchange steps (arrows) achieving proton pumping by bR. The primary proton-transfer step is from the SB to Asp^{85} and corresponds to the spectroscopic L-to-M transition. (**C**) $2mF_{obs} - DF_{calc}$ electron density for the bR active site in its resting conformation. Electron density (gray) is contoured at 1.3σ (σ is the root mean square electron density of the map). W400, W401, and W402 denote water molecules.

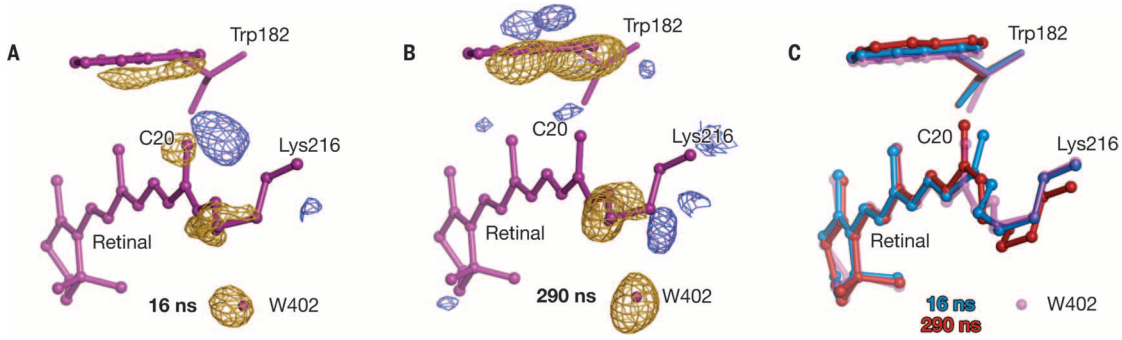

Fig. 2. Early structural changes in the bR photocycle. (**A**) View of the $|F_{obs}|^{light} - |F_{obs}|^{dark}$ difference Fourier electron density map near the retinal for Δt = 16 ns. Blue indicates positive difference electron density; yellow denotes negative difference electron density (contoured at ±3.7σ). The resting-state bR model (purple) was used for phases when calculating this map. Paired negative and positive difference electron densities indicate a sideways movement of the retinal's C20 methyl. (**B**) Identical representation but for the time point Δt = 290 ns. (**C**) Crystallographic models deriving from partial-occupancy refinement for Δt = 16 ns (blue) and Δt = 290 ns (red) superimposed upon the resting bR structure (purple, partially transparent).

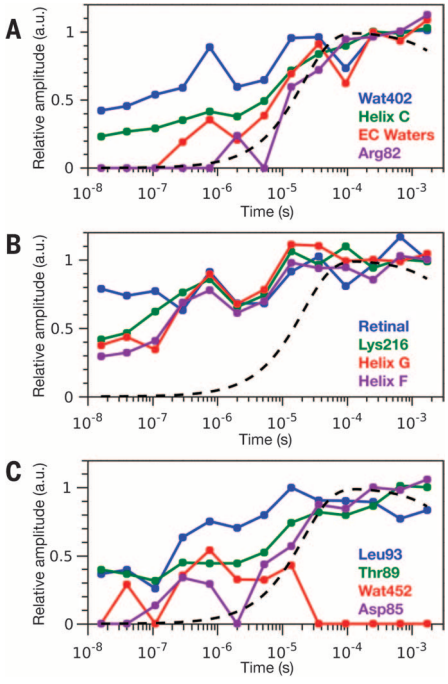

Fig. 3. Relative changes of electron density amplitudes in bR with time. (**A**) Time-dependent root mean square difference electron density amplitudes associated with Wat402 (blue); helix C (green, backbone of Arg^{82}, Ala^{84}, and Asp^{85}); waters 400, 401, and 451 (red, EC waters); and the side chain of Arg^{82} (purple). a.u., arbitrary units. (**B**) Time-dependent amplitudes associated with the retinal (blue), the side chain of Lys^{216} (green), helix G (red, backbone of Ser^{214}, Ala^{215}, and Lys^{216}) and helix F (purple, side chains of Trp^{178} and Trp^{182} and backbone of Arg^{175}). (**C**) Time-dependent amplitudes associated with Leu^{93} (blue), the side chain of Thr^{89} (green), Wat452 (red), and the side chain of Asp^{85} (purple). Amplitudes were averaged over the last four time points and scaled to 1 [except Leu^{93} and Wat452 (*42*)]. Amplitudes for Δt = 95.2 μs, 657 μs, and 1.725 ms are scaled by 2.0, 1.5, and 0.8, respectively (*42*). Linear decomposition of electron density amplitudes shows how these motions are coordinated (fig. S8). The M-state population measured from microcrystalline slurries is indicated for comparison (dashed black line).

A water molecule was built at the Wat452 location in one cryo-trapped L-intermediate structure (*23*) but was not observed in any other L-state study (*24*–*26*). Fourier transform infrared (FTIR) spectroscopy observations have inferred that a transient H-bond interaction of the SB to a water molecule arises in the L-state (*27*, *28*), and Wat452 is the only plausible candidate for this interaction. Computer simulations also establish that a water molecule at this position can channel a proton to Asp^{85} through Thr^{89} (*29*). Another transient water molecule (Wat453), which forms H-bond interactions with the carbonyl oxygen of Lys^{216} and the backbone nitrogen of Gly^{220}, was also predicted from FTIR spectroscopy studies (*30*) and is observed in the difference electron density.

On the EC side of the retinal, the disordering of Wat402 triggers a structural cascade visible from $\Delta t \geq$ 13.8 μs as significant (≥4σ) difference electron density peaks that show the disordering of Wat400 and Wat401 and the ordering of a new water molecule, Wat451, between Asp^{85} and Asp^{212} (Fig. 5 and table S2). Concomitant with these active-site water rearrangements is an increase in the strength of paired negative and positive difference density features along the EC portions of helix C (residues 82 to 89, Fig. 5B), which are modeled as a concerted inward movement of helix C toward helix G (Fig. 5C). These observations are similar to electron density changes recorded in low-temperature trapping studies of the bR L-state (*7*, *24*, *25*), but TR-SFX data show that this inward flex of helix C approaches its maximum amplitude as the SB is deprotonated [i.e., as the M-state population grows (Fig. 3A)]. Protons exchange between consecutive water molecules in the model channel gramicidin A on a subpicosecond time scale (*31*), and the primary proton transfer should be very fast once a structure facilitating this exchange is attained. Consequently, the time required for bR to evolve to a conformation with helix C bent toward helix G is the rate-limiting step that controls the primary proton transfer and explains why it takes microseconds for the SB to be deprotonated.

Breaking the EC connectivity after proton transfer

A key conceptual issue underpinning membrane transport is the nature of the "switch," or more specifically, how the SB breaks access to the EC side of bR after the primary proton transfer to Asp^{85}. This is central to the mechanism of proton pumping because structural changes must prevent Asp^{85} from reprotonating the SB or the photocycle would be futile. A switch may be achieved by breaking the pathway for the reverse proton transfer or by perturbing the chemical environment of key groups to shift the equilibrium in favor of the forward proton-transfer reaction.

Difference electron density features associated with movements of the retinal, helix F (Trp^{182}, Thr^{178}, and Arg^{175}), and helix G (Lys^{216}, Ala^{215}, and Ser^{214}) all show a stepwise increase in strength from Δt = 5.25 to 36.2 μs, which coincides with the primary proton-transfer event (Fig. 3B). We therefore conclude that proton transfer from the SB to Asp^{85} effects a structural change within the retinal, which we model as a displacement of the SB toward the CP by 0.15 Å and of the C20 methyl by 0.21 Å, over the interval 760 ns ≤ $\Delta t \leq$ 36.2 μs. These changes may be due to the retinal being subtly straighter when deprotonated (*32*) or to proton transfer neutralizing the mutual electrostatic attraction between the SB and Asp^{85} (*6*). Both geometric and electrostatic effects increase the separation between the SB and Asp^{85} and would therefore increase the barrier for the reverse proton transfer.

Protein structural changes also hinder the reverse proton transfer from Asp^{85} to the SB. Wat452, which may help mediate the primary proton transfer through Thr^{89} (Fig. 4B), is observed for 40 ns ≤ $\Delta t \leq$ 13.8 μs but is not visible after a proton is transferred to Asp^{85} (Fig. 3C and table S2). An H-bond interaction connecting Thr^{89} to Asp^{85} is also lost after the primary proton-transfer event, with significant (≥4σ) negative difference electron density becoming visible between Oγ of Thr^{89} and Oδ of Asp^{85} for $\Delta t \geq$ 36.2 μs (Fig. 5D, movie S2, and table S2). These

structural changes break the reverse proton-transfer pathway from Asp^{85} to the SB through Thr^{89} and Wat452 while simultaneously increasing the pK_a of Asp^{85}. Thr^{89} moves closer to the retinal in the M state with the H bond from Oγ of Thr^{89} to the SB decreasing from 3.30 Å at 760 ns to 3.04 Å at 36.2 μs and to 2.86 Å at 1.725 ms. This tighter H-bond donor interaction to the deprotonated SB locks Thr^{89} in a conformation that allows the Asp^{85} side chain to rotate and break its connectivity to Thr^{89} while forming a new H-bond interaction with Wat451. In contrast with TR-SFX, FTIR spectroscopy studies at low temperature have predicted a tight Thr^{89}-Asp^{85} H-bond interaction in the M state (*33*), but the complex dynamics of these H-bond interactions may preclude a unique interpretation of spectroscopic observations.

Synchronous with the M-state spectral transition is a displacement of the positively charged head group of Arg^{82} toward the EC (Figs. 3A and 5C), which implies that this movement is triggered by the protonation of Asp^{85}. This rearrangement displaces a positive charge away from Asp^{85} and consequently increases the pK_a of the primary proton acceptor, hindering the reverse proton-transfer reaction (*34*). These structural perturbations also trigger a rearrangement of Glu^{194} and Glu^{204}, which were modeled from $\Delta t \geq 250$ μs. Similar structural changes have been observed for trapped M intermediates and were argued to influence the release of a proton to the EC medium (*34*, *35*). Overall, this sequence highlights structural changes that favor Asp^{85} being protonated and reveal how the SB accessibility to the EC side of the protein is broken after the SB is deprotonated, thereby functionally coupling the primary proton-transfer event to the switch in the bR photocycle.

Structural changes on the CP side of bR

Correlated movements are observed on the CP side of helix F as paired negative and positive difference electron density stacking through Trp^{182}, Thr^{178}, and Arg^{175} (Fig. 6, A and B, and movie S3). As with electron density changes associated with the retinal and near the center of helix G, difference density features on CP portions of helix F arise rapidly but plateau once the SB is deprotonated (Fig. 3B). Structural refinement indicates that the retinal's C20 methyl group is displaced by 1.12 Å toward the CP over the time sequence sampled here, with a corresponding displacement of Trp^{182} of 0.96 Å. The largest Cα displacement is 1.13 Å and occurs for Lys^{216} at Δt = 1.725 ms. In helix F, the Cα atoms of residues 174 to 178 are displaced by only 0.4 Å; therefore, as with cryo-trapped structures of M intermediates (*34*–*37*), TR-SFX does not reveal the large movements of helices E and F that were predicted from bR triple-mutant structures (*32*, *38*). This discrepancy may be reconciled by noting that motions of these helices are severely restricted in the $P6_3$ crystal form because residues 165 and 166 of the E-F loop participate in crystal contacts with residues 232 and 234 of the C terminus (fig. S7). Although larger motions of the CP portions of

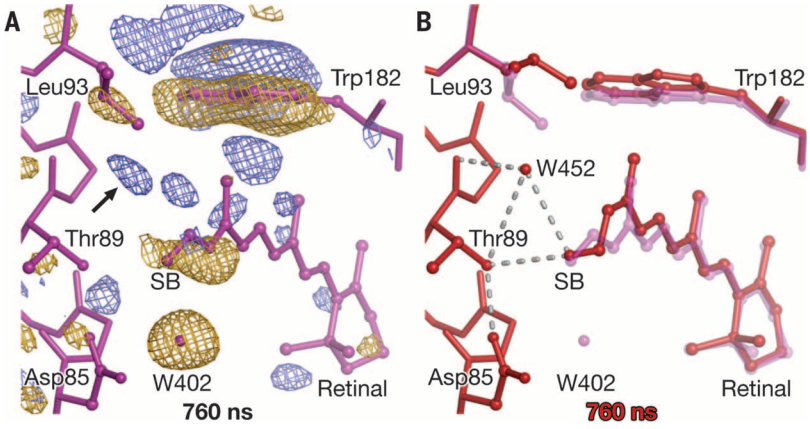

Fig. 4. Pathway for proton transfer from the SB to Asp^{85}. (**A**) View of the $|F_{obs}|^{light} - |F_{obs}|^{dark}$ difference Fourier electron density map (contoured at ±3.1σ) near the retinal for Δt = 760 ns. A positive difference feature (arrow) suggests the ordering of a water molecule (Wat452). (**B**) Crystallographic model for the time point Δt = 760 ns (red) superimposed upon the resting-state model (purple, partially transparent).

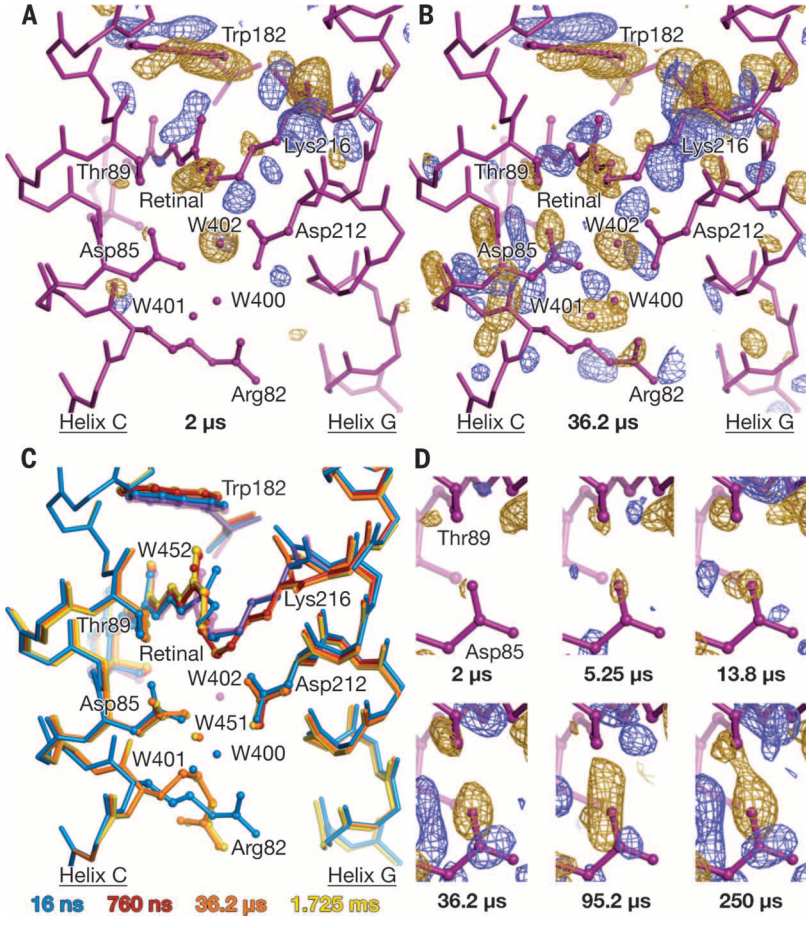

Fig. 5. bR conformation controlling the primary proton transfer event. (**A** and **B**) View of the difference Fourier electron density map immediately to the EC side of the retinal for (A) Δt = 2 μs and (B) Δt = 36.2 μs. All maps are contoured at ±3.5σ. Difference Fourier electron density maps from this viewpoint are shown for all 13 time points in movie S2. (**C**) Crystallographic structural models deriving from partial-occupancy refinement are superimposed upon the resting bR structure (purple, partially transparent) for Δt = 16 ns (blue), 760 ns (red), 36.2 μs (orange), and 1.725 ms (yellow). (**D**) Close-up view of difference electron density across the Asp^{85}-Thr^{89} H bond for the time points Δt = 2 μs, 5.25 μs, 13.8 μs, 36.2 μs, 95.2 μs, and 250 μs. All maps are contoured at ±3.5σ except for Δt = 95.2 μs, which is contoured at ±2.8σ.

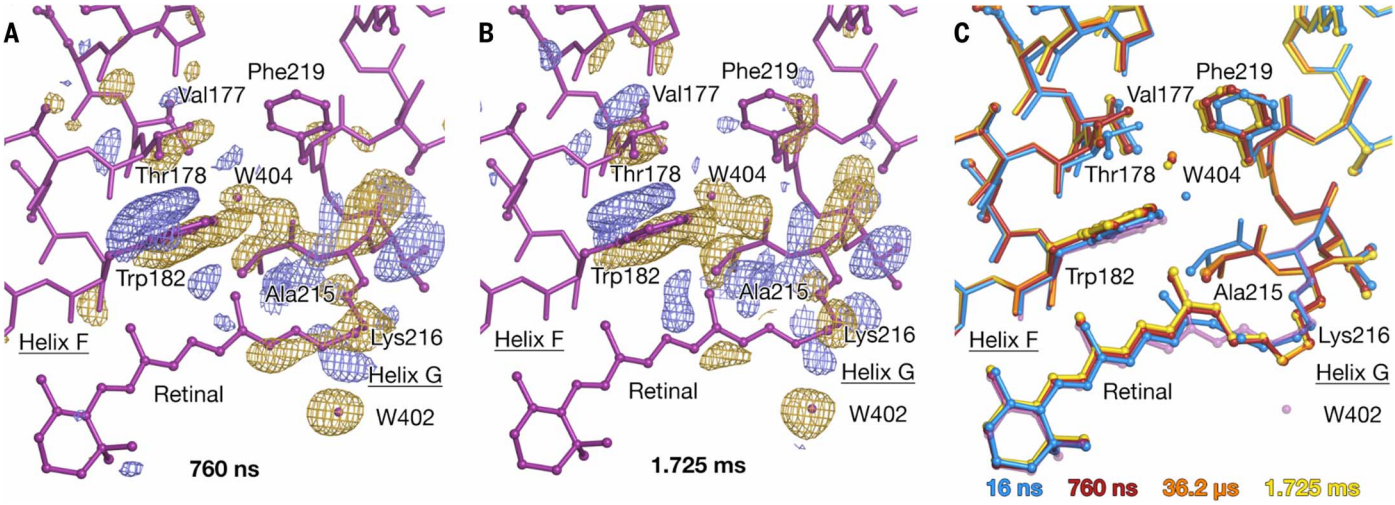

Fig. 6. Conformational changes on the CP side of bR. (**A** and **B**) Close-up view of the difference Fourier electron density map immediately to the CP side of the retinal for (A) Δt = 760 ns and (B) Δt = 1.725 ms. All maps are contoured at ±3.5σ. Difference Fourier electron density maps from this viewpoint are shown for all 13 time points in movie S3. (**C**) Crystallographic structural models deriving from partial-occupancy refinement are superimposed upon the resting bR structure (purple, partially transparent) for Δt = 16 ns (blue), 760 ns (red), 36.2 µs (orange), and 1.725 ms (yellow).

helices E and F arise later in the bR photocycle (*39*, *40*), these structural changes cannot be critical for the mechanism of proton pumping. This is because these motions are suppressed in 3D crystals yet the photocycle is similar to that of bR in the purple membrane (fig. S3), and the Asp^{96}→Gly^{96}/ Phe^{171}→Cys^{171}/Phe^{219}→Leu^{219} bR triple mutant is constitutively open to the CP yet is able to pump protons (*41*).

Mechanistic overview

Retinal isomerization reorients the SB proton into a hydrophobic cavity while breaking its H bond to Wat402, both of which lower the proton affinity of the SB (*14*). An initially twisted retinal becomes planar within 290 ns, causing Trp^{182} and Leu^{93} to be displaced toward the cytoplasm and allowing a water molecule to order between Leu^{93}, Thr^{89}, and the SB in the L state. H-bond interactions from the protonated SB to Wat452 or Thr^{89} create a pathway for proton transfer to Asp^{85} (Fig. 4B) and explain how the SB makes contact with Asp^{85} despite having been turned toward the CP by photoisomerization. A steric clash between Cε of Lys^{216} and Wat402 dislodges this water molecule, triggering the collapse of the water-mediated H-bond network on the EC side of bR. This allows helix C to bend toward helix G approximately 10 µs after photoactivation and raises the pK_a of Asp^{85} to the point where it may spontaneously accept a proton from the SB. Once a proton is transferred, the Asp^{85}-Thr^{89} H bond is lost (Fig. 5D), thus breaking the SB connectivity to the EC side of the protein. Consequently, diffraction data spanning five orders of magnitude in time reveal how structural changes in bR achieve unidirectional membrane transport half a century after Jardetzky first proposed the alternating access framework obeyed by all membrane transporters (*1*).

REFERENCES AND NOTES

1. O. Jardetzky, *Nature* **211**, 969–970 (1966).
2. J. Tenboer *et al.*, *Science* **346**, 1242–1246 (2014).
3. T. R. Barends *et al.*, *Science* **350**, 445–450 (2015).
4. K. Pande *et al.*, *Science* **352**, 725–729 (2016).
5. U. Haupts, J. Tittor, D. Oesterhelt, *Annu. Rev. Biophys. Biomol. Struct.* **28**, 367–399 (1999).
6. R. Neutze *et al.*, *Biochim. Biophys. Acta* **1565**, 144–167 (2002).
7. C. Wickstrand, R. Dods, A. Royant, R. Neutze, *Biochim. Biophys. Acta* **1850**, 536–553 (2015).
8. Y. Matsui *et al.*, *J. Mol. Biol.* **324**, 469–481 (2002).
9. V. I. Borshchevskiy, E. S. Round, A. N. Popov, G. Büldt, V. I. Gordeliy, *J. Mol. Biol.* **409**, 813–825 (2011).
10. V. Borshchevskiy *et al.*, *Acta Crystallogr. D Biol. Crystallogr.* **70**, 2675–2685 (2014).
11. R. Neutze, R. Wouts, D. van der Spoel, E. Weckert, J. Hajdu, *Nature* **406**, 752–757 (2000).
12. K. Hirata *et al.*, *Nat. Methods* **11**, 734–736 (2014).
13. H. Luecke, H. T. Richter, J. K. Lanyi, *Science* **280**, 1934–1937 (1998).
14. M. Sheves, A. Albeck, N. Friedman, M. Ottolenghi, *Proc. Natl. Acad. Sci. U.S.A.* **83**, 3262–3266 (1986).
15. C. H. Chang, R. Jonas, R. Govindjee, T. G. Ebrey, *Photochem. Photobiol.* **47**, 261–265 (1988).
16. S. Hayashi, E. Tajkhorshid, K. Schulten, *Biophys. J.* **83**, 1281–1297 (2002).
17. A. N. Bondar, S. Fischer, S. Suhai, J. C. Smith, *J. Phys. Chem. B* **109**, 14786–14788 (2005).
18. K. Edman *et al.*, *Nature* **401**, 822–826 (1999).
19. K. Nass *et al.*, *J. Synchrotron Rad.* **22**, 225–238 (2015).
20. B. Schobert, J. Cupp-Vickery, V. Hornak, S. Smith, J. Lanyi, *J. Mol. Biol.* **321**, 715–726 (2002).
21. H. G. Khorana, *Proc. Natl. Acad. Sci. U.S.A.* **90**, 1166–1171 (1993).
22. G. A. Jeffrey, *An Introduction to Hydrogen Bonding* (Oxford Univ. Press, 1997).
23. T. Kouyama, T. Nishikawa, T. Tokuhisa, H. Okumura, *J. Mol. Biol.* **335**, 531–546 (2004).
24. A. Royant *et al.*, *Nature* **406**, 645–648 (2000).
25. K. Edman *et al.*, *J. Biol. Chem.* **279**, 2147–2158 (2004).
26. J. K. Lanyi, B. Schobert, *J. Mol. Biol.* **365**, 1379–1392 (2007).
27. A. Maeda *et al.*, *Biochemistry* **41**, 3803–3809 (2002).
28. A. Maeda, F. L. Tomson, R. B. Gennis, S. P. Balashov, T. G. Ebrey, *Biochemistry* **42**, 2535–2541 (2003).
29. A. N. Bondar, J. Baudry, S. Suhai, S. Fischer, J. C. Smith, *J. Phys. Chem. B* **112**, 14729–14741 (2008).
30. A. Maeda *et al.*, *Biochemistry* **42**, 14122–14129 (2003).
31. R. Pomès, B. Roux, *Biophys. J.* **71**, 19–39 (1996).
32. S. Subramaniam, R. Henderson, *Nature* **406**, 653–657 (2000).
33. H. Kandori *et al.*, *Proc. Natl. Acad. Sci. U.S.A.* **98**, 1571–1576 (2001).
34. H. Luecke, B. Schobert, H. T. Richter, J. P. Cartailler, J. K. Lanyi, *Science* **286**, 255–260 (1999).
35. H. Luecke *et al.*, *J. Mol. Biol.* **300**, 1237–1255 (2000).
36. H. J. Sass *et al.*, *Nature* **406**, 649–653 (2000).
37. M. T. Facciotti *et al.*, *Biophys. J.* **81**, 3442–3455 (2001).
38. T. Wang *et al.*, *Structure* **21**, 290–297 (2013).
39. M. H. Koch *et al.*, *EMBO J.* **10**, 521–526 (1991).
40. M. Andersson *et al.*, *Structure* **17**, 1265–1275 (2009).
41. J. Tittor *et al.*, *J. Mol. Biol.* **319**, 555–565 (2002).
42. Materials and methods are available as supplementary materials on *Science* Online.

ACKNOWLEDGMENTS

We thank K. Oshimo for her help in culturing *Halobacterium salinarum* and members of the Engineering Team of RIKEN SPring-8 Center—especially Y. Shimazu, K. Hata, N. Suzuki, and T. Kin—for technical support. XFEL experiments were conducted at BL3 of SACLA, with the approval of the Japan Synchrotron Radiation Research Institute (JASRI) (proposal numbers 2014B8051, 2015A8047, and 2015B8054). Crystals were checked for diffraction at BL41XU of SPring-8 with the approval of JASRI (proposal number 2015A1119). This work was supported by the X-ray Free-Electron Laser Priority Strategy Program (Ministry of Education, Culture, Sports, Science and Technology of Japan) and partially by the Strategic Basic Research Program (JST) and RIKEN Pioneering Project Dynamic Structural Biology. We acknowledge computational support from the SACLA High Performance Computing system and the Mini-K supercomputer system. R.N. acknowledges financial support from the Swedish Research Council (grants VR 349-2011-6485 and 2015-00560), the Swedish Foundation for Strategic Research (grant SSF SRL 10-0036), and the Knut and Alice Wallenberg Foundation (grant KAW 2012.0284). A.R. acknowledges financial support from the French National Research Agency (grant ANR-11-JSV5-0009). T.Ki. is supported by Japan Society for the Promotion of Science KAKENHI grant 15H05476. P.N. acknowledges support from the European Community's Seventh Framework Program (FP7/2007-2013) under grant 290605 (PSI-FELLOW/COFUND). J.S. acknowledges support from the Swiss National Science Foundation project grant (SNF 31003A_159558). G.S. acknowledges support from the Swiss National Science Foundation (grant SNF 310030_153145) and the NCCR-MUST/FAST program. C.S. is supported by National Research Foundation of Korea (grants NRF-2015R1A5A1009962 and NRF-2016R1A2B3010980) and the POSCO Green Science program. A.-N.B. acknowledges support in

part from the Excellence Initiative of the German Federal and State Governments provided via the Freie Universität Berlin, the Deutsche Forschungsgemeinschaft (DFG) through the Collaborative Research Center SFB1078 project C4, as well as computing time from the Freie Universität Berlin and from the North-German Supercomputing Alliance (HLRN). M.M. acknowledges financial support from the Exploratory Research for Advanced Technology of the JST. Author contributions: S.I., R.N., and E.N. conceived the research; T.T., T.A., A.Y., J.K., R.T., E.N., P.N., and J.S. prepared microcrystals; S.M., S.K., and M.M. prepared purple membrane; E.N., C.S., R.N., M.K., and K.T. designed the experimental setup; M.K., T.Ki., T.No., S.O., and J.D. contributed the pump laser setup; E.N., T.T., R.T., T.A., A.Y., J.K., T.Ho., E.M., P.N., M.S., C.S., D.N., R.D., Y.K., T.S., D.I., T.F., Y.Y., B.J., T.Ni., K.O., M.F., C.W., R.A., C.S., P.B., J.S., and R.N. performed data collection; M.K., T.Ki., and T.No. performed time-resolved visible absorption spectroscopy; C.W. and R.N. analyzed the spectral data; T.Na. and O.N. performed data processing; A.R. and E.N. refined the intermediate structures; A.-N.B. performed computations; K.T., C.S., T.Ka., T.Ha., Y.J., and M.Y. developed the SFX systems at SACLA; and R.N., C.W., E.N., A.R., M.K., and T.Na. wrote the paper with input from all authors. Coordinates and structure factors have been deposited in the Protein Data Bank with IDs 5B6V (bR resting state), 5B6W (Δt = 16 ns), 5H2H (Δt = 40 ns), 5H2I (Δt = 110 ns), 5H2J (Δt = 290 ns), 5B6X (Δt = 760 ns), 5H2K (Δt = 2 μs), 5H2L (Δt = 5.25 μs), 5H2M (Δt = 13.8 μs), 5B6Y (Δt = 36.2 μs), 5H2N (Δt = 95.2 μs), 5H2O (Δt = 250 μs), 5H2P (Δt = 657 μs), and 5B6Z (Δt = 1.725 ms). Raw diffraction images have been deposited in the Coherent X-ray Imaging Data Bank (accession ID 53).

SUPPLEMENTARY MATERIALS

www.sciencemag.org/content/354/6319/1552/suppl/DC1
Materials and Methods
Figs. S1 to S9
Tables S1 and S2
References (*43*–*76*)
Movies S1 to S3

28 June 2016; accepted 21 November 2016
10.1126/science.aah3497

TOPOLOGICAL MATTER

Majorana bound state in a coupled quantum-dot hybrid-nanowire system

M. T. Deng,[1,2] S. Vaitiekėnas,[1,3] E. B. Hansen,[1] J. Danon,[1,4] M. Leijnse,[1,5] K. Flensberg,[1] J. Nygård,[1] P. Krogstrup,[1] C. M. Marcus[1]*

Hybrid nanowires combining semiconductor and superconductor materials appear well suited for the creation, detection, and control of Majorana bound states (MBSs). We demonstrate the emergence of MBSs from coalescing Andreev bound states (ABSs) in a hybrid InAs nanowire with epitaxial Al, using a quantum dot at the end of the nanowire as a spectrometer. Electrostatic gating tuned the nanowire density to a regime of one or a few ABSs. In an applied axial magnetic field, a topological phase emerges in which ABSs move to zero energy and remain there, forming MBSs. We observed hybridization of the MBS with the end-dot bound state, which is in agreement with a numerical model. The ABS/MBS spectra provide parameters that are useful for understanding topological superconductivity in this system.

As condensed-matter analogs of Majorana fermions—particles that are their own antiparticles (*1*)—Majorana bound states (MBSs) are anticipated to exhibit non-Abelian exchange statistics, providing a basis for naturally fault-tolerant topological quantum computing (*2*–*7*). In the past two decades, the list of potential realizations of MBSs has grown from even-denominator fractional quantum Hall states (*8*) and *p*-wave superconductors (*9*) to topological insulator-superconductor hybrid systems (*10*), semiconductor-superconductor (Sm-S) hybrid nanowire systems (*11*–*21*), and artificially engineered Kitaev chains (*22*–*24*). Sm-S hybrid systems have received particular attention because of ease of realization and a high degree of experimental control. Experimental signatures of MBS in Sm-S systems have been reported (*25*–*29*), typically consisting of zero-bias conductance peaks in tunneling spectra appearing at finite magnetic field.

In a confined normal conductor-superconductor system, Andreev reflection will give rise to discrete electron-hole states below the superconducting gap—Andreev bound states (ABSs). Given the connection between superconducting proximity effect and ABSs, zero-energy MBSs in Sm-S hybrid nanowires can be understood as a robust merging of ABSs at zero energy, thanks in part to the presence of strong spin-orbit interaction (SOI) (*11*–*13*, *15*, *16*). However, not all zero-energy ABSs are MBSs. For instance, in the nontopological or trivial phase, ABSs can move to zero energy at a particular Zeeman field, giving rise to a zero-bias conductance peak, and then split again at higher fields, indicating a switch of fermion parity (*30*). On the other hand, zero-energy MBSs in short wires may also split as a function of chemical potential or Zeeman field (*14*). In this case, the difference between topological MBSs in a finite-length wire and trivial ABSs is whether the states are localized at the wire ends or not (*17*). We will use the term "MBSs" to refer to ABSs that are to a large degree localized at the wire ends and would evolve into true topological MBSs as the wire becomes longer. We also will use the term "topological phase in a finite-length wire" to refer to the regime in which MBS appears. The similarities between trivial ABS zero-energy crossings and MBS in a finite-length wire can be subtle (*13*, *15*, *16*, *30*, *31*). Several obstacles have prevented a detailed experimental study of the ABS-MBS relation to date, including a soft proximity-induced gap (*18*), the difficulty of tuning the chemical potential of the hybrid nanowire, and disorder in the wire and tunneling barrier.

In this work, we investigated MBSs and their emergence from coalescing ABSs, using tunneling spectroscopy through quantum dots at the end of epitaxial hybrid Sm-S nanowires. We observed gate-controlled hybridization of the MBSs with the bound state in the end dot, finding excellent agreement between experiment and numerical models. The epitaxial Sm-S interface induces a hard superconducting gap (*32*, *33*), whereas the partial coverage by the epitaxial superconductor allows tuning of the chemical potential and yields a high critical field (*34*), both crucial for realizing MBSs.

Hybrid nanowire with end dot

Our devices were made of epitaxial InAs/Al nanowires (Fig. 1A) (*32*). Wurtzite InAs nanowires were first grown to a length of 5 to 10 μm by means of molecular beam epitaxy, followed by low-temperature epitaxial growth of Al. Two or three facets of the hexagonal InAs core were covered by Al (Fig. 1B) (*32*). The nanowires were then deposited onto a degenerately doped silicon/silicon oxide substrate. Transene-D Al etch was used to selectively remove the Al from the end of the wire, which was then contacted by titanium/gold (Ti/Au, 5/100 nm), forming a normal (non-superconducting) metal lead. Five devices were investigated. Data from four devices, denoted 1 to 4, are reported in the main text, and data from a fifth device, denoted 5, are reported in (*35*). For device 1, the unetched end of the nanowire section was contacted by titanium/aluminum/vanadium (Ti/Al/V, 5/20/70 nm), and global back gate and local side gates were used to control the electron density in the wire. A quantum dot was formed in the 150-nm bare InAs wire segment between the Ti/Au normal contact and the epitaxial Al shell, owing to disorder or band-bending (*33*). Fabrication details for the other devices, each slightly different, are given in (*35*). Micrographs of all devices accompany transport data. Except where noted, the magnetic field B was applied parallel to the

[1]Center for Quantum Devices and Station Q Copenhagen, Niels Bohr Institute, University of Copenhagen, 2100 Copenhagen, Denmark. [2]State Key Laboratory of High Performance Computing, National University of Defense Technology, 410073, Changsha, P. R. China. [3]Department of Physics, Freie Universität Berlin, Arnimallee 14, 14195 Berlin, Germany. [4]Niels Bohr International Academy, Niels Bohr Institute, University of Copenhagen, 2100 Copenhagen, Denmark. [5]Division of Solid State Physics and NanoLund, Lund University, Box 118, S-22100, Lund, Sweden.
***Corresponding author. Email: marcus@nbi.dk**

Science

A three-dimensional movie of structural changes in bacteriorhodopsin

Eriko Nango, Antoine Royant, Minoru Kubo, Takanori Nakane, Cecilia Wickstrand, Tetsunari Kimura, Tomoyuki Tanaka, Kensuke Tono, Changyong Song, Rie Tanaka, Toshi Arima, Ayumi Yamashita, Jun Kobayashi, Toshiaki Hosaka, Eiichi Mizohata, Przemyslaw Nogly, Michihiro Sugahara, Daewoong Nam, Takashi Nomura, Tatsuro Shimamura, Dohyun Im, Takaaki Fujiwara, Yasuaki Yamanaka, Byeonghyun Jeon, Tomohiro Nishizawa, Kazumasa Oda, Masahiro Fukuda, Rebecka Andersson, Petra Båth, Robert Dods, Jan Davidsson, Shigeru Matsuoka, Satoshi Kawatake, Michio Murata, Osamu Nureki, Shigeki Owada, Takashi Kameshima, Takaki Hatsui, Yasumasa Joti, Gebhard Schertler, Makina Yabashi, Ana-Nicoleta Bondar, Jörg Standfuss, Richard Neutze and So Iwata

Science **354** (6319), 1552-1557.
DOI: 10.1126/science.aah3497

Snapshots of bacteriorhodopsin

Bacteriorhodopsin is a membrane protein that harvests the energy content from light to transport protons out of the cell against a transmembrane potential. Nango *et al.* used timeresolved serial femtosecond crystallography at an x-ray free electron laser to provide 13 structural snapshots of the conformational changes that occur in the nanoseconds to milliseconds after photoactivation. These changes begin at the active site, propagate toward the extracellular side of the protein, and mediate internal protonation exchanges that achieve proton transport.

Science, this issue p. 1552